International Journal of Fatigue 68 (2014) 56–66

Contents lists available at ScienceDirect

International Journal of Fatigue

journal homepage: www.elsevier.com/locate/ijfatigue

Cohesive zone modeling of fatigue crack propagation assisted by gaseous hydrogen in metals

C. Moriconi, G. Hénaff *, D. Halm

Department of Physics and Mechanics of Materials, Institute Pprime (UPR 3346), CNRS, ENSMA, Université de Poitiers, BP40109, F-86961 Futuroscope Chasseneuil Cedex, France

ARTICLE INFO

Article history:
Received 19 February 2014
Received in revised form 11 June 2014
Accepted 13 June 2014
Available online 23 June 2014

Keywords:
Cohesive zone
Hydrogen embrittlement
Finite element analysis
Constitutive law

ABSTRACT

Experimental studies in a hydrogenous environment indicate that hydrogen leads to a modification of deformation and damage mechanisms at the fatigue crack tip in metals, resulting in a significant decrease of crack propagation resistance. This study aims at building a model of these complex phenomena in the framework of damage mechanics, and to confront it with the results of fatigue crack propagation tests in high pressure hydrogen on a 15-5PH martensitic stainless steel. A cohesive zone model is implemented in the finite element code ABAQUS. A specific traction-separation law is developed, which is suitable for cyclic loadings, and whose parameters depend on local hydrogen concentration. Furthermore, hydrogen diffusion in the bulk material takes into account the influence of hydrostatic stress and trapping. Simulated fatigue crack propagation rates in hydrogen are compared to experimental measurements. The model ability to assess the respective contributions of the different damage mechanisms in the degradation of the crack resistance of the 15-5PH steel is discussed.

1. Introduction

The role of hydrogen in deformation and damage processes taking place at the crack tip has been commonly evoked to account for environmentally-assisted fatigue crack growth in metals exposed to an hydrogenous environment [1], although the mechanisms responsible for the observed loss of crack growth resistance, which can be tremendous in some cases, were not fully elucidated. This issue meets a renewed interest due to the forthcoming shortage of fossil energy sources and environmental concerns which motivate the development of hydrogen-based energy infrastructure. Indeed, the materials which would be used in such infrastructures and that may contain crack-like defects would have to withstand a direct exposure to high pressure of gaseous hydrogen in conjunction with the application of a cyclic mechanical loading. This question is generally tackled from the point of view of the compatibility of a given metal with gaseous hydrogen [2]. However the question of compatibility of a given material is not straightforward and one has to define the boundary of safe operation conditions. Therefore, the integrity of the hydrogen transport and storage structures cannot be guaranteed without a sound understanding of the damage mechanisms prevailing at a crack tip in a gaseous hydrogen environment and an identification of the controlling factors. From a more fundamental point of view, an improved understanding of hydrogen interactions with deformation and damage mechanisms at the tip of a fatigue crack is needed.

With this perspective, the Pprime Institute has undertaken, a couple of years ago, the development of a new test bench named Hycomat in order to investigate the mechanical behavior of structural materials under high pressure of gaseous environments [3,4]. Hycomat is composed of a specially designed autoclave assembled to a servohydraulic loadframe. The maximum operating pressure is 40 MPa, and the highest temperature in the autoclave is 150 °C. Cyclic loadings can be applied with different frequencies on Compact Tension specimens. A computerized system is associated to control the testing process by monitoring the crack length by means of a potential drop technique. However, such experiments are costly and the results are extremely complex to analyze, for instance when considering different pressure/load frequency conditions as [4]. This is the reason why it was decided at the same time to develop a model based on coupled effects between mechanical cyclic loading and hydrogen diffusion. A specifically designed cohesive zone approach, in which hydrogen directly affects the traction-separation law, is investigated. The objective is not only to simulate the experimental results or provide accurate fatigue life predictions, but also to provide a numerical tool that can be used to analyze and understand the different pressure and/or frequency effects on fatigue crack growth rates. This paper

* Corresponding author.
E-mail address: gilbert.henaff@ensma.fr (G. Hénaff).

http://dx.doi.org/10.1016/j.ijfatigue.2014.06.007
0142-1123/

Nomenclature

ΔK	stress intensity factor amplitude (MPa $\times$ m$^{1/2}$)
R	load ratio
δ_n	normal component of the displacement in the cohesive zone
$\delta_{n,max}$	maximum value of δ_n
δ_t	tangential component of the displacement in the cohesive zone
φ	thermodynamic potential of the traction-separation law
D	damage variable, ranging from 0 to 1
D_m	monotonic part of the damage variable
D_c	cyclic part of the damage variable
k	initial normal tension stiffness,
k_{comp}	compression stiffness
k_t	tangent stiffness
δ_0	dimensionless parameter
$\vec{T}(T_n, T_t)$	cohesive traction vector
$T_{n,in}$	value of the normal cohesive traction component at damage initiation
f_c	threshold function for the onset of the cyclic damage
f_m	threshold function for the onset of the monotonic damage
c_c	constant related to the cyclic damage initiation
c_m	constant related to the monotonic damage initiation
m_c	constant controlling the cyclic damage progressivity
n_c	cyclic exponent
N_L	density of hydrogen lattice sites
N_T	density of hydrogen trap sites
m_m	constant controlling the monotonic damage progressivity
n_m	monotonic exponent
$r_{p,cyc}$	size of the cyclic plastic zone
Y	thermodynamic force associated with the damage parameter D
F_{sta}	mean value of the applied cyclic loading
ΔF	amplitude of the applied cyclic loading
Δg_b^0	Gibbs free energy difference between a microstructural interface (crystallographic planes, grain boundary,...) and the bulk material
C_H	hydrogen concentration
θ	hydrogen coverage rate
C_L	hydrogen concentration in lattice
C_T	hydrogen concentration in traps,
D_L	the lattice diffusivity coefficient,
$\overline{V}_h$	mean molar volume of hydrogen
σ_h	hydrostatic stress

presents the principles of the model considered and preliminary results from numerical computations.

2. A cohesive zone model for cyclic loading

2.1. Selection of the type of model

Literature offers various possibilities to model damage at a crack tip at different scales. Thermodynamic approaches [5] can indicate if hydrogen embrittlement is likely to occur but they do not explicitly address the damage process, especially at the crack scale. Meanwhile hydrogen-assisted fracture can be envisaged from an atomistic point of view [6]. Some attempts have been made to fill the gap between these two types of envision [7]. On the opposite, global approaches, based on continuum mechanics, such as J-integral and CTOD methods, micromechanical models such as the Gurson model [8], as well as more recent phenomenological numerical approaches, such as the eXtended Finite Element Method (X-FEM), developed by Belytschko et al. [9,10], have been successfully applied to address fracture problems without most generally considering a specific role of hydrogen. Among these approaches, the cohesive zone models (CZM), based on the original work of Dugdale [11] and Barenblatt [12], deserve attention. Indeed the cohesive zone represents the area near the crack tip (the so-called process zone) by a relation between cohesive stress and crack opening displacement, called the Traction-Separation Law (TSL). Moreover the cohesive zone models have the advantage of being flexible, considering that the TSL shape is a matter for phenomenological issues. One main limitation in this kind of approach resides in the fact that it usually requires a predefined crack path. The usual traction-separation laws include linear [13] , multilinear [14,15], polynomial [16] or exponential [17] laws. Furthermore it has to be noticed that they have been applied with a certain success to account for hydrogen-assisted cracking under monotonic or static loading [18–21]. However, the traction-separation laws suffer from the absence of stiffness degradation under cyclic loading, with the noticeable exceptions in [22–24].

As mentioned in the previous section, the main goal of this study is to develop a simulation tool that can predict the fatigue crack growth under different hydrogen exposure conditions, that is to say different pressures, loading frequencies and possibly various temperatures, but not, at this stage, to predict the crack path within a component submitted to a complex loading. Therefore the limitation related to a predefined crack path is not really an issue. Meanwhile the capability of CZM to describe hydrogen-assisted fracture under static and monotonic loading is attractive. Therefore a CZM approach was selected in this study, with the development of a specific TSL, established within the framework of the Thermodynamics of Irreversible Processes and that could address the various issues listed here above. Indeed this TSL has firstly to describe fatigue crack propagation. Furthermore, the parameters of this TSL are dependent on hydrogen coverage in an attempt to account for the detrimental influence of hydrogen on fatigue crack growth [4]. The basic idea is that the damage process is localized within the cohesive zone, which means that the bulk material surrounding this zone is not damaged despite the elasto-plastic cyclic deformation endured. The TSL is described by 2 vectors, namely a crack opening displacement vector and a cohesive stress vector. At this first stage, the model will be developed in a 2D framework.

The mechanical behavior of the bulk will be described by conventional elasto-plastic constitutive laws while the local hydrogen concentrations will be determined from constitutive equations for hydrogen and trapping, including the effects of traps.

2.2. Development of a specific traction-separation law

2.2.1. Monotonic and cyclic damage

Cohesive zone models describe the area near the crack tip – called the "process zone" – by a local relation between the cohesive traction vector and the opening displacement, which is the difference between the top and bottom crack lip displacements [17,25–27]. In a 2D framework, the opening displacement is defined by its normal (δ_n) and tangential (δ_t) components. The cohesive law is introduced via the thermodynamic potential φ:

$$\varphi = \frac{1}{2}k(1-D)\frac{\langle\delta_n\rangle^2}{\delta_0} + \frac{1}{2}k_{comp}\frac{\langle-\delta_n\rangle^2}{\delta_0} + \frac{1}{2}k_t\frac{\delta_t{}^2}{\delta_0} \quad (1)$$

where $\langle\ldots\rangle$ stands for the positive part.

The scalar D is the damage internal variable, ranging from 0 to 1. The constants k, k_{comp} and k_t represent the initial normal tensile stiffness, the compressive stiffness and the tangential stiffness, respectively, while δ_0 is a dimensionless parameter.

The cohesive traction vector $\vec{T}(T_n, T_t)$ is derived from the potential φ by the following relations (state laws), according to the general principles of Thermodynamics of Irreversible Process [28]:

$$T_n = \frac{\partial \varphi}{\partial \delta_n} = k(1-D)\frac{\langle \delta_n \rangle}{\delta_0} + k_{comp}\frac{\langle -\delta_n \rangle}{\delta_0} \tag{2}$$

and

$$T_t = \frac{\partial \varphi}{\partial \delta_t} = k_t \frac{\delta_t}{\delta_0} \tag{3}$$

In a similar way, the thermodynamic force Y associated with the damage internal variable D is defined as follows:

$$Y = -\frac{\partial \varphi}{\partial D} = \frac{1}{2}k\frac{\langle \delta_n \rangle^2}{\delta_0} \tag{4}$$

The damage internal variable D is defined as the maximum value of two distinct sources of damage, namely a monotonic source D_m and a cyclic contribution D_c:

$$D = \max(D_m, D_c) \tag{5}$$

It has to be noticed that the two contributions D_m and D_c vary separately, according to the yield conditions $f_c = 0$ and $f_m = 0$, respectively, where the yield functions f_c and f_m are defined as follows:

$$f_c = \int_0^t \langle \dot{Y} \rangle (1-D_c)^{n_c} d\tau - (c_c + m_c D_c) \tag{6}$$

$$f_m = \int_0^t \dot{Y}_{max}(1-D_m)^{n_m} d\tau - (c_m + m_m D_m), \tag{7}$$

where c_c and c_m are constant. The parameters m_c and m_m control the progressivity of the variation of D_c and D_m, respectively, and as a consequence the variation of D (cf. Eq. (5)). The exponents n_c and n_m control the separation energy. In Eq. (7), Y_{max} (and $\dot{Y}_{max}$ its rate) is thus defined as the maximum value of the thermodynamic force Y from the initial time $t = 0$ to the current time (see Fig. 1).

In the present case, a *non associated* framework is used to define the evolution of the damage variable: the evolution of the cyclic part of the damage variable is found to follow the normality rule with respect to a dissipation potential $\phi(Y)$, function of the thermodynamic force (see [29] for a general presentation of the irreversible thermodynamics tools). A simple choice for ϕ ($\phi(Y) = Y$) leads to the following expression for $\dot{D}_c$:

$$\dot{D}_c = \dot{\lambda}_c \frac{\partial \phi}{\partial Y} = \dot{\lambda}_c \tag{8}$$

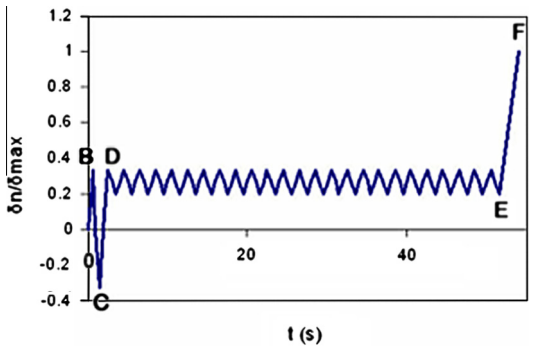

Fig. 1. History of the opening displacement amplitude, leading to Fig. 2.

where $\dot{\lambda}_c$ is a damage multiplier, whose expression stems from the consistency equation $\dot{f}_c = 0$:

$$\dot{D}_c = \frac{k}{m_c}(1-D_c)^{n_c}\langle \delta_n \rangle \langle \dot{\delta}_n \rangle \tag{9}$$

Note the normality rule postulated here is relative to the maximum dissipation hypothesis and is known, when associated with the convexity property of ϕ, to assure *a priori* the thermodynamic admissibility.

Similarly, the normality rule is valid for the monotonic part of the damage variable:

$$\dot{D}_m = \dot{\lambda}_m \frac{\partial \phi}{\partial Y} = \dot{\lambda}_m \tag{10}$$

When the "monotonic" threshold $f_m = 0$ is satisfied, the consistency equation $\dot{f}_m = 0$ leads to the evolution of D_m:

$$\dot{D}_m = \frac{k}{m_m}(1-D_m)^{n_m}\langle \delta_{n,max} \rangle \langle \dot{\delta}_{n,max} \rangle \tag{11}$$

where $\delta_{n,max}$ stands for the maximum value of δ_n from the start of the loading to present time. Eq. (9) shows that D_c increases when δ_n and its time derivative are both strictly positive. Note that D_c and D_m are not allowed to decrease, according to the irreversible nature of damage. Fig. 2 represents a plot of the normal cohesive stress T_n (normalized by maximum value T_{max}) versus the normal opening displacement δ_n (normalized by maximum value δ_{max}), under a prescribed displacement amplitude, shown in

The normal cohesive stress T_n is limited by an exponential-shaped curve related to the monotonous contribution D_m. Initially, both D_m and D_c are equal to zero, and T_n varies linearly with respect to δ_n. As soon as either one of thresholds $f_c = 0$ or $f_m = 0$ is reached, D_m or D_c increases, leading to a variation of damage variable D (cf. Eq. (5)), up to point B in and Fig. 2. Then, when the opening displacement is negative (point C), the yield conditions $f_c = 0$ and $f_m = 0$ are no longer satisfied, and D_m and D_c do not evolve. Note that very high stiffness corresponds to the term k_{comp} in the expression of the thermodynamic potential. As soon as the constant amplitude cyclic loading is started (point D), D_m remains unchanged, while D_c keeps on increasing, becoming larger than D_m, up until reaching point E. As a consequence the stiffness gradually decreases. Finally, when the opening displacement is increased up to point F, D_m becomes greater than the cyclic contribution D_c; the cohesive stress then follows the exponential-shaped curve.

2.2.2. Influence of hydrogen

In order to take into account the influence of hydrogen on fatigue crack growth, the parameters of the traction-separation law

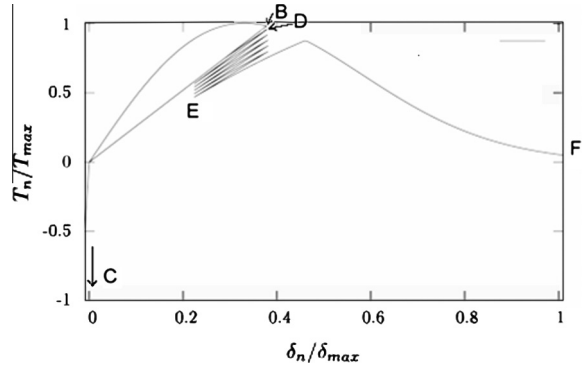

Fig. 2. Normal cohesive stress T_n (normalized by T_{max}) as a function of the normal opening displacement δ_n (normalized by δ_{max}).

are supposed to depend on hydrogen coverage rate θ [11], ranging from 0 to 1, which is defined as a function of local hydrogen concentration in the material C_H and the Gibbs free energy difference between any microstructural interface (crystallographic planes, grain boundary,...) and the bulk material Δg_b^0:

$$\theta = \frac{C_H}{C_H + \exp\left(\frac{-\Delta g_b^0}{RT}\right)} \tag{12}$$

where C_H is the hydrogen concentration.

According to Olden et al. [30], and using the relationship initially proposed by Serebrinsky et al. [31] on the basis of first principle calculations by Jiang and Carter [32], it is furthermore assumed that an increase in hydrogen coverage leads to a similar decrease of the initial stiffness k, the traction corresponding to the damage initiation (controlled by c_m for the monotonic damage and c_c for the cyclic one) and the progression of both damage types (related to constants m_m and m_c), as follows:

$$\frac{k(\theta)}{k(0)} = \frac{m_m(\theta)}{m_m(0)} = \frac{m_c(\theta)}{m_c(0)} = \frac{c_m(\theta)}{c_m(0)} = \frac{c_c(\theta)}{c_c(0)} = f(\theta), \tag{13}$$

$$\text{where}: f(\theta) = 1 - 1.0467\theta + 0.1687\theta^2, \tag{14}$$

and where $k(0)$, $m_c(0)$, $m_m(0)$, $c_c(0)$ and $c_m(0)$ are the values of the corresponding parameters in the absence of hydrogen ($\theta = 0$). Fig. 3 presents the normalized traction-separation law for various values of hydrogen coverage θ under monotonic loading. As the hydrogen coverage increases, the softening process occurs at a smaller normal opening displacement while the maximum value of normal tensile strength decreases.

2.3. Implementation of the proposed CZM in ABAQUS package

The ABAQUS commercial software package considers 2D, 3D or axisymmetric cohesive elements. However the choice in traction-separation laws is extremely limited (bi-linear or exponential laws). In addition these elements are not suited to cyclic loading. Indeed the damage laws only consider the maximal value of the opening displacement $\delta_{m,max}$ encountered during the loading as a criterion to make the damage variable vary. Hence under a cycling loading under constant maximum opening the value of the damage parameter would not vary. It was then decided to introduce the CZM model described in the previous section as a UEL (User Element) user subroutine. Indeed ABAQUS offers the possibility to develop customized finite elements. During computations this subroutine is called at each time increment for selected elements. In the present case it consists in the calculation of the different steps

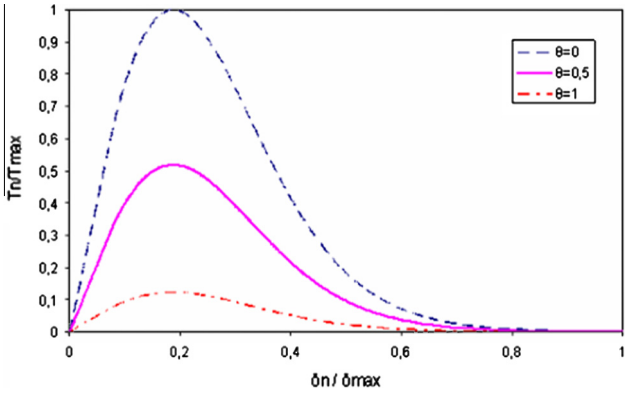

Fig. 3. Normalized traction-separation law under monotonous loading for different values of hydrogen coverage.

of the proposed TSL for a 2D cohesive element with 4 nodes and 2 integration points for the mechanical behavior. Temperature is defined as an extra degree of freedom at each node. This allows the use of the «coupled temperature-displacement» procedure in ABAQUS. Indeed, thanks to the analogy between heat and hydrogen diffusion equations (see Table 1), the local hydrogen concentration is assimilated to the temperature degree of freedom.

Coupling between the mechanical behavior and the hydrogen diffusion can thus be modeled by the means of a coupled temperature/displacement procedure. The subroutine UMATHT, available in ABAQUS, allows one to define defining the thermal properties of the material and, by analogy, the hydrogen diffusion equation.

It is assumed hydrogen diffuses in the bulk elements and not directly in the cohesive ones (due to their infinitesimal thickness). However hydrogen in the bulk influences the cohesive elements through their common nodes. When the cohesive element breaks, it is assumed that hydrogen diffusion is almost instantaneous. From a numerical point of view, this assumption permits to ensure the boundary condition of constant hydrogen concentration at the crack tip, when the crack grows.

3. Simulations of fatigue crack propagation assisted by gaseous hydrogen

The previous section focused on the development of a specific traction-separation law suited for cyclic loadings and taking into account the deleterious influence of hydrogen on the cohesion energy, according to the HEDE (Hydrogen-Enhanced DEcohesion) theory, originally proposed by Oriani [35]: it is assumed that the presence of hydrogen in the lattice alters the strength of atomic bonds and as a consequence and consequently reduces the cohesion energy. Prior to simulating fatigue crack growth in CT specimens, it is necessary to deal with the hydrogen diffusion in the bulk material, as well as its plastic behavior.

3.1. Hydrogen concentration in the bulk material

It has been shown that the proposed TSL is modified by the local enrichment in hydrogen. The question is then to determine this enrichment with respect to the boundary conditions. This question is treated using the diffusion equation originally proposed by Sofronis and McMeeking [33] and subsequently modified by Krom et al. [34] to describe the diffusion of hydrogen in stress fields in the bulk material:

$$\frac{\partial C_L}{\partial t} + \frac{\partial C_T}{\partial t} - \vec{\nabla}\cdot(D_L\vec{\nabla}C_L) + \vec{\nabla}\cdot\left(\frac{D_L C_L \overline{V}_h}{RT}\vec{\nabla}\sigma_h\right) = 0 \tag{15}$$

where C_L stands for the hydrogen concentration in lattice, C_T the hydrogen concentration in traps, D_L is the lattice diffusivity coefficient, $\overline{V}_h$ is the mean molar volume of hydrogen and σ_h corresponds to the hydrostatic stress.

In order to obtain the derivative of C_T with respect to time, the theory developed by Oriani [35] and Johnson and Lin [36,37] is used to distinguish the different hydrogen atom populations, namely diffusible atoms and trapped atoms. The concentration of trapped hydrogen C_T is thus derived from the lattice concentration C_L by the following equations:

$$C_T = \frac{N_T}{1 + \frac{1}{K_T C_L}} \tag{16}$$

where $K_T = \exp\left(\frac{-W_B}{RT}\right)$ represents the equilibrium constant while W_B stands for the binding enthalpy. Furthermore the C_L and C_T concentrations are related to the hydrogen coverage rates θ_L and θ_T of interstitial and trapping sites, respectively, by means of the following relations:

Table 1
Parallel between heat and mass diffusion equation.

	Heat equation $\rho C_P \frac{\partial T}{\partial t} + div\vec{J}_q + r_q = 0$	Mass diffusion equation $\frac{\partial C}{\partial t} + div\vec{J}_m + r_m = 0$
Nodal quantity (unit)	Temperature T (K)	Hydrogen concentration C (g/mol)
Heat/mass flux (unit)	$\vec{J}_q$ (W/m^2)	$\vec{J}_m$ (g m/mol/s)
Heat/mass source (unit)	r_q (W/m^3)	r_m (g/mol/s)

$$C_T = \theta_T N_T \qquad C_L = \theta_L N_L \tag{17}$$

N_L and N_T are respectively the densities (per unit volume) of hydrogen lattice and trap sites. Once C_L is known by solving Eq. (15), C_T is obtained from Eq. (16), in which the value of N_T depends on the equivalent plastic strain ε_p [33]: $\log N_T = 23.26 - 2.33 \cdot \exp(-5.5\varepsilon_p)$, and the value of the binding enthalpy W_B is taken equal to −60 kJ/mol., according to the work by Kumnick and Johnson [38].

3.2. Elasto-plastic constitutive law

The cyclic stress–strain behavior of the 15-5PH steel used in this study has been previously studied in the laboratory by Hamon [39]. It was then shown that a non-linear kinematic hardening can account for the observed behavior in an accurate manner. For computations in ABAQUS, the use of the "coupled temperature-displacement" procedure requires the development of a UMAT user subroutine. The UMAT subroutine allows the user to define a specific behavior for a given finite element. In the subroutine programming, the stress tensor and the tangent matrix have to be defined at each integration point at the end of the time increment. The links between the UEL, UMATHT and UMAT subroutines are specified in Fig. 4.

3.3. FE analysis: geometry and boundary conditions

3.3.1. Geometry, meshing and computational method

As one of the objectives is to compare predicted and measured fatigue crack growth rates, the first FE analysis was performed on the basis of a CT specimen geometry similar to that used in experiments. This geometry is presented in Fig. 5.

Apart from the cohesive elements used in the crack plane, 2D plane-stress elements are used to mesh the specimen. As shown in Fig. 5, a progressive mesh refinement is used in the crack vicinity. Ancillary computations have been carried out in order to investigate a possible influence of the mesh size by considering three mesh sizes at the crack tip, namely: 0.4, 1 and 2 μm. As the results show no influence of the mesh size, it was decided to use the largest value (2 μm).

It was furthermore decided to confine the cyclic damage D_c in cohesive elements to the cyclic plastic zone. In other words, there is no damage in the cohesive elements as long as they are not included in the plastic zone. This condition is handled by imposing no cyclic damage evolution in the cohesive elements whose adjacent bulk elements do not undergo plastic hardening.

In addition, a special fracture criterion was used for cohesive elements. Indeed it was considered that failure of a cohesive element occurs as soon as the global damage variable reaches a critical value (0.999), or when the element has endured a significant cyclic damage ($D_c = 0.6$ for instance) but does no longer increases because the plastic deformation in the adjacent element does not vary. This last condition avoids the failure of a cohesive element after very long calculations because the cyclic damage does not longer vary.

3.3.2. Boundary conditions and loading

According to Feih [40], in the half CT specimen model, additional nodes are introduced in the crack line in order to define the cohesive elements. During the deformation of the specimen, the nodes on the superior and inferior sides progressively move from each other. The displacement of these nodes in the crack growth direction has then to then be blocked. When only this boundary condition is applied, the nodes of the crack line are allowed to move in the direction perpendicular to the crack. A preliminary analysis by Feih [40] indicates that the half specimen modeled in this way does not fully account for the behavior of the entire specimen. According to this author, given the symmetry of the test piece, the corresponding nodes on each side of the crack plane have the same displacement and the cohesive elements do not withstand any shear loading. This condition is insured in ABAQUS by using the «*EQUATION» command for each cohesive node couple. In addition, in order to avoid any solid body motion, one node, located on the opposite side with respect to the notch, is blocked along the crack growth direction (Fig. 5).

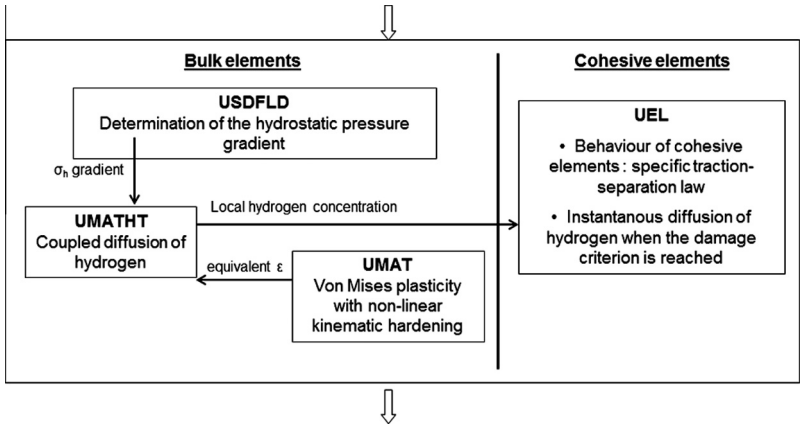

Fig. 4. Relations between links between the UEL, UMATHT and UMAT subroutines.

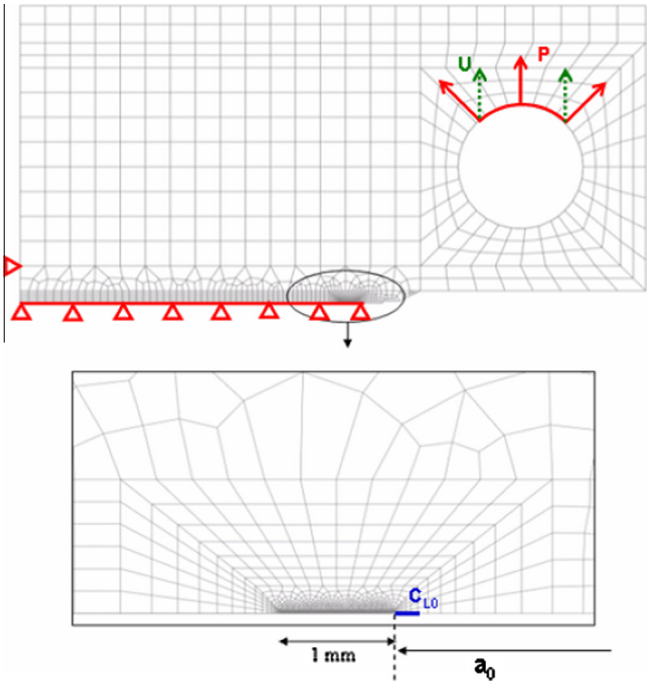

Fig. 5. Geometry, meshing, boundary conditions and loading of a half CT40 specimen. The distance a_0 represents the initial crack length determined from the loading axis, P is the pressure imposed on the superior quarter of the pin hole (which can be alternatively changed into a displacement condition) and C_{L0} is the imposed lattice hydrogen concentration at the crack tip.

A pressure is imposed on the superior part of the pin hole as shown in Fig. 5. More precisely, in order to reduce the computation duration, it was decided to perform computations for selected values of the stress intensity factor amplitude ΔK at a given load ratio. The load to be applied is then determined and the simulation is performed until the crack gets out of the refined mesh zone. The calculation is then stopped by the UEL subroutine. The crack advance Δa as a function of the number of cycles is analyzed and the crack growth rate da/dN is derived. Thus a given simulation provides a (ΔK, da/dN) data point that can be compared to experimental data.

The applied load F is decomposed into a mean part F_{sta} and an amplitude $\Delta F/2$ ($F = F_{sta} + \Delta F/2x \cos\omega t$, where ω is the pulsation and t the time). The load amplitude is determined accordingly with ASTM-E467 standard [41]:

$$\Delta F = \frac{B\sqrt{W}\Delta K}{f(\alpha)} \tag{18}$$

where : $f(\alpha)$

$$= \frac{(2+\alpha)}{(1-\alpha)^{3/2}}\left(0.886 + 4.6\alpha - 13.32\alpha^2 + 14.72\alpha^3 - 5.6\alpha^4\right) \tag{19}$$

The derived values of the mean load F_{sta} and the load amplitude ΔF are then used to determine the pressure that has to be applied on the bore of the pin hole. As shown in Fig. 6, the applied load signal is triangular in shape. In order to accurately describe the loading cycle, the time increment is limited to 1/12 of the loading period.

The boundary conditions relative to hydrogen are placed on a few nodes in the crack tip vicinity. The hydrogen concentration at these nodes is assumed to be constant and equal to C_{L0} during loading. The choice of such boundary conditions is justified by the 2D approach developed in this model. Indeed the hydrogen profile through the CT specimen thickness estimated on the basis of the Fick's second law indicates that time is not sufficient for hydrogen to diffuse towards the mid-thickness for testing at 20 Hz (frequency applied in the simulations). In addition the area of interest for coupled hydrogen diffusion is located ahead of the crack tip. It is then not necessary to set a given value for C_{L0} along the entire notch. The value of C_{L0} is determined by means of Sievert's law using data for pure iron [42] (since no value for the parameters of the Sievert's law can be found in the literature for martensitic steels, it is assumed they do not much differ from that of ferrite). Thus, at an external hydrogen pressure of 9 MPa, Sievert's law provides a solubility: $S = 1.96 \times 10^{22}$. By assuming that the surface concentration is equivalent to the solubility, one obtains the boundary conditions (hydrogen concentration at the notch root) as a function of external hydrogen pressure.

3.3.3. Identification of the TSL parameters

The identification of the TSL parameters has been conducted on the basis of experimental data obtained in air on the 15-5PH steel under study [3], while such an identification should be conducted by considering data obtained in an inert environment. However it should be noted that in the da/dN range explored here, the environmental effect in air is expected to be limited and more particularly not controlled by hydrogen effects at the crack tip [43]. By considering a single datapoint (for example, here, at $\Delta K = 10$ MPa$\sqrt{m}$) from the experimental da/dN curve, the values reported in Table 2 were obtained for the different parameters according to the procedure described hereafter.

The initial tensile stiffness k_n has to be very high (to avoid artificial compliance caused by the presence of cohesive elements). As a consequence, a value of 10^7 MPa has been selected as in [23]. As regards the parameters controlling the monotonic damage parameter D_m, namely m_m, C_m and n_m, the exponential shape of the proposed TSL has to be recalled (see Fig. 2). This shape is derived from the definition of D as the maximum of the respective contribution of D_m and D_c, and from the definition of D_m. The consequence is that the separation energy under cyclic loading, corresponding to the area under the TSL, is limited by the separation energy under monotonic loading determined by the m_m, C_m and n_m parameters. The value of this energy must be high enough to allow the separation energy under cyclic loading to reach the crack growth rate measured experimentally.

Besides the initial threshold for damage C_m is actually related to the normal cohesive stress at the initiation of damage $T_{n,\,in}$ by:

$$C_m = \frac{1}{2}\frac{T_{n,in}^2}{k_n} \tag{20}$$

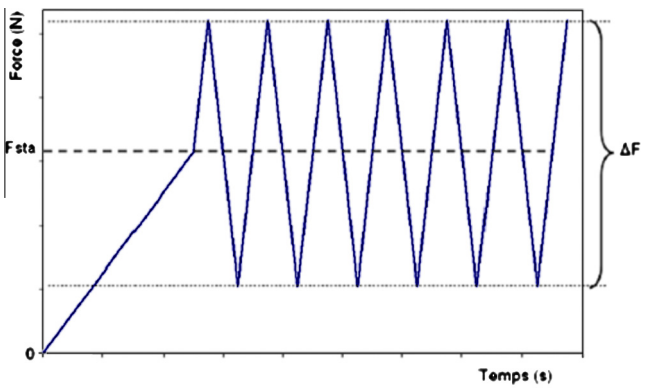

Fig. 6. Applied load as a function of time.

Table 2
Values of the different parameters of the TSL.

k_n	m_m	C_m	m_c	C_c	n_m	n_c
10^7 MPa	450 J/m^2	20 J/m^2	60,000 J/m^2	500 J/m^2	2.6	1

In a first approach, the value of C_m was fixed such that $T_{n,in}$ was slightly lower than the yield strength of the material. By considering $T_{n,in} = 750$ MPa, Eq. (20) yields: $C_m = 28$ J/m^2. The value of was finally approximated as 20 J/m^2.

The m_m and n_m parameters control the fracture energy under monotonic loading in the sense that the higher their value, the higher the separation energy.

Besides, the value of k_n being fixed, a higher value of m_m induces a higher value of the maximum normal cohesive stress T_{max}. Now a high value of T_{max} induces in turn a large amount of plastic deformation in the adjacent elements of the bulk. The value of T_{max}, and therefore of m_m, have to be limited in order to avoid huge plastic deformations. As regards the exponent n_m, it controls the softening stage of the TSL without significantly altering the value of T_{max}. The values of these two parameters reported in Table 2 were selected in order to achieve a sufficiently high value of the fracture energy while keeping a moderate value of T_{max}. For a monotonic loading, a preliminary calculation showed that, when the damage variable D reaches its critical value ($D = 0.999$), the dissipated energy is about 29 J/m^2. This value is comparable to that reported by Scheider et al. [44] for a tensile loading on a low-alloy high strength steel.

As concerns the "cyclic" parameters of the TSL, the value of c_c is selected such as that cyclic damage variable D_c does not vary before the start of cyclic loading. The value reported in Table 2 was derived from preliminary computations. The value of the energy per surface area m_c controls the variation of the cyclic damage D_c, and as a consequence the kinetics of the degradation of the stiffness of the cohesive elements under cyclic loading. Then, from a single (ΔK, da/dN) data point, and having determined the values of k_n, m_m, c_m, n_m and c_c, the value of m_c given in Table 2 can be derived to fit the selected experimental value of crack growth rate for the corresponding ΔK. A parametric study indicated that the value of n_c has almost no influence of the TSL. In a first approach its value was fixed to 1.

Finally, literature [43] provides some rough estimates for the dissipated energy at the crack tip when fatigue crack grows. However this energy can be dissipated either by separation or by plasticity and [43] does not distinguish these contributions. Since dissipation by plasticity is not confined in a few elements, its contribution must be important. That is why it can only by concluded that the energy dissipated by the cohesive elements under cyclic loading (here lower than 29 J/m^2) is much lower than the values found in [43].

4. Results and discussion

4.1. Fatigue crack growth without hydrogen

Fig. 7 presents the results of different computations performed for two load ratio values, namely $R = 0.1$ and $R = 0.7$, at two different ΔK values using the parameter values given in Table 2. It can be seen that a higher value of ΔK induces a higher crack growth rate. In addition, several cohesive elements can fail during the initial monotonic loading to the mean load and during the first quarter of cycle. Indeed, in the model, this local failure is due to the fact that the value of the monotonic damage D_m is immediately close to 1. The lower the value of the exponent n_m is, the higher the number of failed elements during this loading stage is. Furthermore it appears that the curves obtained at two different load ratio for a given ΔK value are close. This is because the cyclic damage varies only in the cyclic plastic zone which is controlled by the ΔK value.

In order to get a better view of the respective role of the two damage terms, Fig. 8 presents the profiles of these variables as a function of the distance from the initial crack tip. It can be seen that after the initial loading stage (Fig. 8a), the monotonic damage variable reaches a value close to 0.3 in several cohesive elements at the crack tip while the cyclic damage remains null. The size of the zone affected by the monotonic loading is about 240 μm. This value is slightly higher than the value estimated by conventional Irwin's relationship as shown in Fig. 8a (dashed line). For $\Delta K = 20$ MPa $\times$ m$^{1/2}$, $R = 0.1$, this relation yields a value of 140 μm. This difference is related to the C_m damage threshold parameter.

After 422 cycles (Fig. 8b), the crack has propagated over several failed cohesive elements. The zone affected by the monotonic damage has nearly the same size than at the start of cyclic loading. Moreover a cyclic process zone where the cyclic damage is nonzero with a size of about 30 μm is present at the crack tip. This size is in agreement with the size estimated using fracture mechanics relationships:

$$r_{p,cyc} = \frac{1}{2\pi}\left(\frac{\Delta K}{2\sigma_y}\right) \tag{21}$$

which leads to a value of $r_{p,cyc} = 28$ μm consistent with the size predicted by the model (Fig. 8b; the size has to be measured from the actual crack tip).

Finally, a steady state fatigue crack growth rate value is derived from the computed data as presented in Fig. 7 for given ΔK and R values. This allows to construct da/dN curves such as those presented in Fig. 9 and to compare them to experimental data. It comes out in Fig. 10 that the proposed model, based on cohesive elements dedicated to cyclic damage is able to accurately predict fatigue crack growth rates over a broad range of ΔK values and for two distinct values of the R load ratio in the absence of hydrogen. Now it has to be recalled that the model was also originally designed to account for the effect of hydrogen on fatigue crack growth. The next section addresses this point. The results of the simulation are compared to experimental data obtained at a load frequency of 20 Hz. In spite of this high value, Fig. 10 clearly shows the deleterious effect of hydrogen.

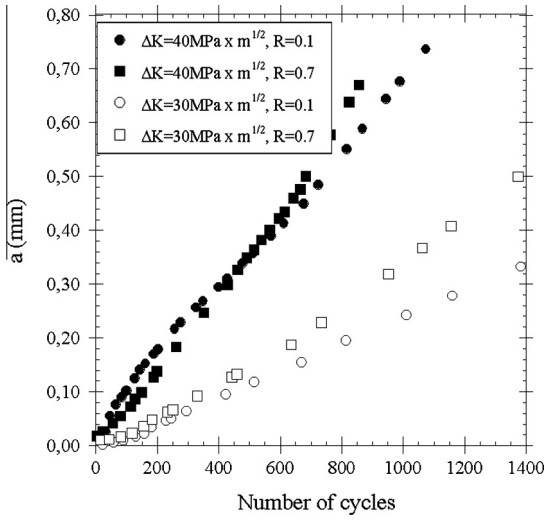

Fig. 7. Crack length as a function of the number of cycles N at $R = 0.1$ and $R = 0.7$, $\Delta K = 30$ MPa $\times$ m$^{1/2}$ and $\Delta K = 40$ MPa $\times$ m$^{1/2}$).

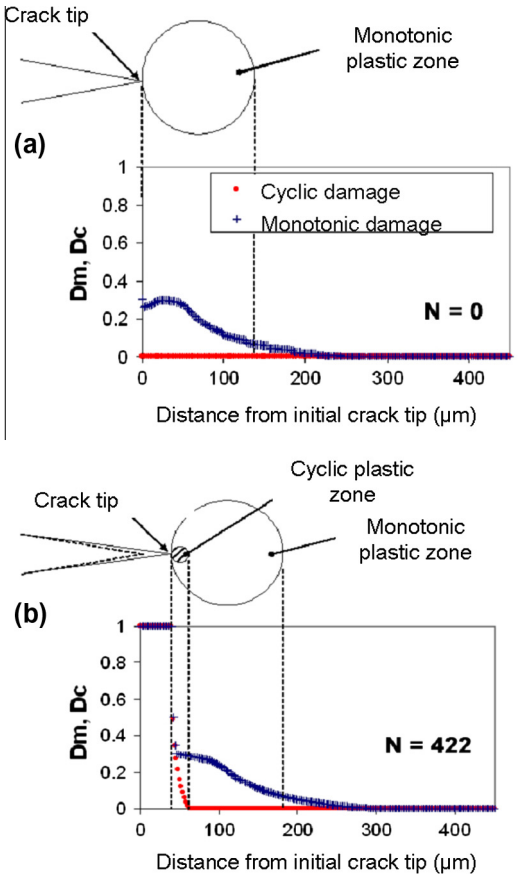

Fig. 8. Profiles of monotonic and cyclic damage as a function of the distance from the initial crack tip ($\Delta K = 20$ MPa $\times$ m$^{1/2}$, $R = 0.1$) at different number of cycles: $N = 0$ (a), $N = 422$ (b).

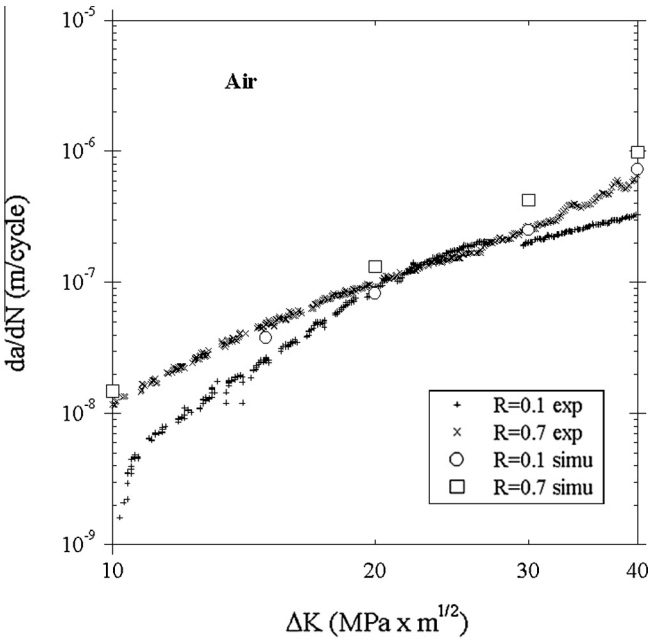

Fig. 9. Simulated *da*/*dN* curves compared to experimental data in air in a 15-5PH martensitic stainless steel.

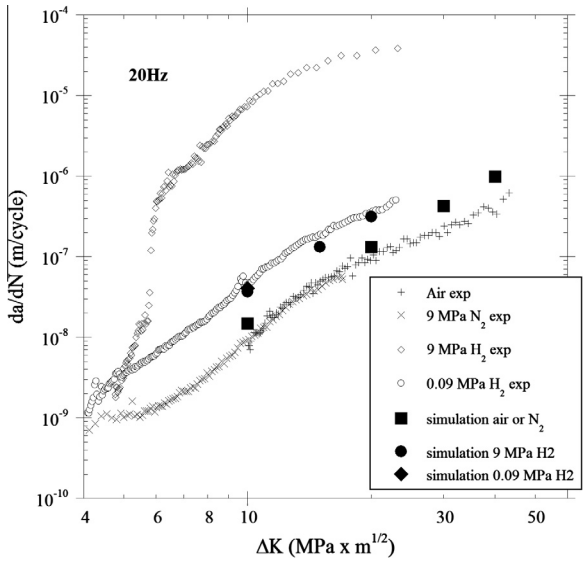

Fig. 10. Simulated *da*/*dN* curves under a gaseous hydrogen pressure of 9 MPa at 20 Hz in a 15-5PH martensitic stainless steel – comparison with experimental curves under air and under hydrogen pressure of 0.09 MPa and 9 MPa.

4.2. Fatigue crack growth under gaseous hydrogen

The simulations of propagation under gaseous hydrogen are performed using the same procedure. In a first approach, the elasto-plastic constitutive law is assumed to be insensitive to the presence of dissolved hydrogen in the bulk. The influence of hydrogen pressure and loading frequency are more precisely addressed in the next sections. A special attention is furthermore paid to the respective role of trapped and diffusible hydrogen.

On the basis of simulations carried out at $\Delta K = 10$, 15 and 20 MPa $\times$ m$^{1/2}$ for a gaseous hydrogen pressure of 9 MPa, the *da*/*dN* curves presented in Fig. 10 are obtained.

It can be seen that, under a gaseous hydrogen pressure of 9 MPa and a loading frequency of 20 Hz, the model predicts a fatigue crack growth enhancement of a factor of 2.5 ratio for the various ΔK values considered. Furthermore additional simulations performed for a hydrogen pressure of 0.09 MPa indicate that, for $\Delta K = 10$ MPa $\times$ m$^{1/2}$ and a frequency of 20 Hz, the predicted fatigue crack growth rate is extremely close to that obtained at a pressure of 9 MPa, so that the corresponding data points are superimposed in Fig. 10.

Therefore, if the model seems to be able to account for the fatigue crack growth behavior under low hydrogen pressure, a huge difference is noticed at high pressure between predicted and experimental fatigue crack growth rates, especially at high ΔK values. This suggests that some of the ingredients introduced in the model are not sufficient to account for the tremendous fatigue crack growth enhancement observed at 9 MPa of gaseous hydrogen. In order to get further insights into this issue, the influence of hydrogen pressure, ΔK level and load frequency are analyzed in the following sections.

4.2.1. Influence of hydrogen pressure

In order to investigate the influence of hydrogen pressure on fatigue crack growth rates, the profile of the hydrogen coverage rate θ ahead of the crack tip is considered. Actually this coverage rate is determined from the total concentration $C(\theta)$ and the lattice concentration C_L (θ_L). A calculation performed at a loading frequency of 20 Hz and at $\Delta K = 10$ MPa $\times$ m$^{1/2}$ at two gaseous hydrogen pressure, 0.09 MPa and 9 MPa and after 250 loading cycles is

shown in Fig. 11. This number of cycles corresponds with a crack advance of about 30 μm at both pressures.

The examination of Fig. 11 indicates that, in a zone of a few micrometers that is affected by hydrogen ahead of the crack tip, the coverage rates are higher at 9 MPa. According to Sievert's law the surface concentration is 10 times higher than at 0.09 MPa. The same ratio is found in the coverage rate θ_L at the crack tip. Moreover, a significant contribution of trapped hydrogen is noticed. For a pressure of 9 MPa, at this ΔK value and loading frequency, the distance affected by the presence of hydrogen is about 4 μm, corresponding with two cohesive elements. At a lower pressure, only the cohesive element immediately placed at the crack tip is affected by hydrogen diffusion. According to Oriani theory [35], the trapped hydrogen is in equilibrium with the interstitial lattice hydrogen. As a consequence hydrogen can only be trapped in areas where interstitial hydrogen can diffuse, which is actually observed in Fig. 11. While the enrichment is significant, it has to be noticed that for this exposure and loading condition, the measured crack growth rate is 3.7×10^{-2} μm/cycle, corresponding to 0.74 μm/s at 20 Hz. Therefore the crack growth is too fast for hydrogen to diffuse over a distance of 2–4 μm, even for a pressure of 9 MPa. It is noteworthy that in the case under consideration, as the penetration distance of diffusible hydrogen is small, the gradient of hydrostatic stress in the diffusion equation (Eq. (15)) has almost no influence.

4.2.2. Influence of ΔK level

In Fig. 12 are presented the coverage rate profiles determined for two ΔK values, namely $\Delta K = 10$ MPa $\times$ m$^{1/2}$ and $\Delta K = 20$ MPa $\times$ m$^{1/2}$, at a loading frequency of 20 Hz and a gaseous hydrogen pressure of 9 MPa after 250 cycles.

First it has to be noticed that the value of the coverage rate θ_L does not depend on the ΔK level since it mainly depends on the surface concentration at the crack tip which in turn depends on the hydrogen pressure. Then it appears that the concentration of trapped hydrogen is higher at $\Delta K = 20$ MPa $\times$ m$^{1/2}$. As a consequence the total coverage rate is higher, which is in agreement with the results reported by Sofronis and McMeeking [33]. Indeed these authors showed that, using coupled diffusion equation, an increase in the loading rate promotes the trapping of hydrogen. As regards the penetration distance, at $\Delta K = 10$ MPa $\times$ m$^{1/2}$ a distance of about 4 μm is affected by hydrogen. However, at $\Delta K = 20$ MPa $\times$ m$^{1/2}$ only the first cohesive element, that means a distance of 2 μm, is affected by hydrogen diffusion. This difference can be accounted for by the difference in crack growth rates. Indeed at $\Delta K = 20$ MPa $\times$ m$^{1/2}$, fatigue crack growth rates are 8 times higher than at $\Delta K = 10$ MPa $\times$ m$^{1/2}$. As a consequence the time available for hydrogen to diffuse is much less and the distance affected by hydrogen is smaller.

One can therefore conclude that the higher the ΔK value, the higher the contribution of trapped hydrogen and the shorter the distance affected by hydrogen are.

4.2.3. Influence of cyclic loading frequency

In order to examine the influence of loading frequency, a numerical simulation of the crack tip hydrogen profile has been carried after 250 cycles at $\Delta K = 10$ MPa $\times$ m$^{1/2}$ at a lower frequency, namely 0.2 Hz. The results are reported and compared to those obtained at 20 Hz in Fig. 13. The profiles are compared for a similar crack advance, namely 30 μm, which corresponds with 142 cycles at 0.2 Hz and 250 cycles at 20 Hz.

The results presented here indicate that at a low frequency of 0.2 Hz, the zone affected by hydrogen penetration is larger than at high frequency. This higher penetration distance is due to the longer time available for lattice diffusion. Indeed, by using conventional diffusion equations and a diffusion coefficient of the order of 10^{-12} m^2/s, this distance at 0.2 Hz is estimated at 6.3 μm while it is 100 times smaller at 20 Hz. The computational results yield similar orders of magnitude. However it has to be noticed that the coverage rate is strongly affected by frequency. In addition the quantity of trapped hydrogen has a major contribution in the coverage rate. However it seems that even in that case the hydrostatic stress term has a minor role. Indeed the hydrogen profile presented in Fig. 13 does not present a peak in coverage rate located ahead of the crack tip that could be indicative of a significant contribution of this term.

5. Concluding remarks on the capacities and limitations of the proposed model

The proposed model is a cohesive zone model, with a traction-separation law specially designed for cyclic loading and accounting

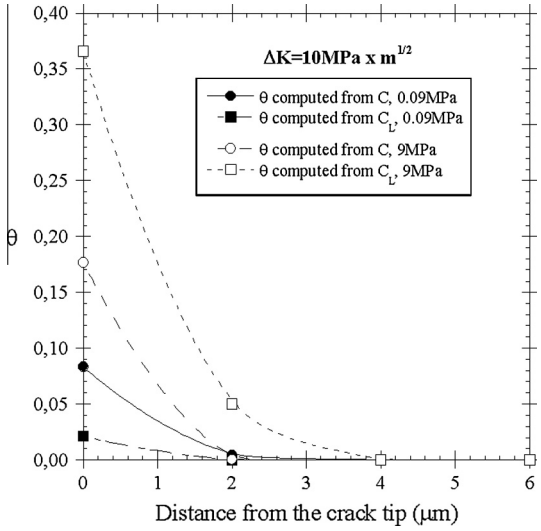

Fig. 11. Hydrogen coverage rate, determined after 250 cycles from the total concentration $C(\theta)$ and the lattice concentration C_L (θ_L), at a loading frequency of 20 Hz and at $\Delta K = 10$ MPa $\times$ m$^{1/2}$ at two gaseous hydrogen pressure, 0.09 MPa and 9 MPa, plotted as a function of the distance from the crack tip.

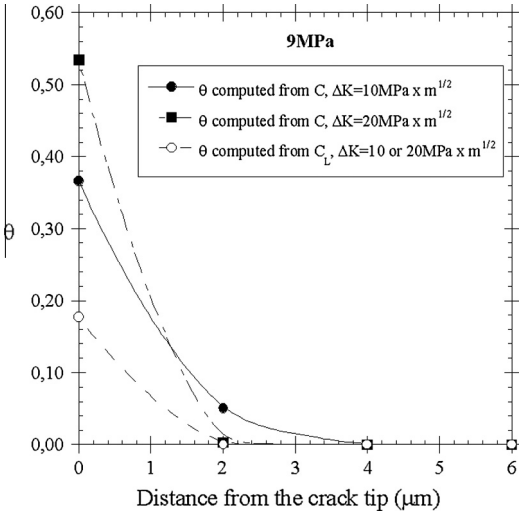

Fig. 12. Hydrogen coverage rate, determined after 250 cycles from the total concentration $C(\theta)$ and the lattice concentration C_L (θ_L), at a loading frequency of 20 Hz and two ΔK values, namely $\Delta K = 10$ MPa $\times$ m$^{1/2}$ and $\Delta K = 20$ MPa $\times$ m$^{1/2}$ at a loading frequency of 20 Hz, a gaseous hydrogen pressure of 9 MPa, plotted as a function of the distance from the crack tip.

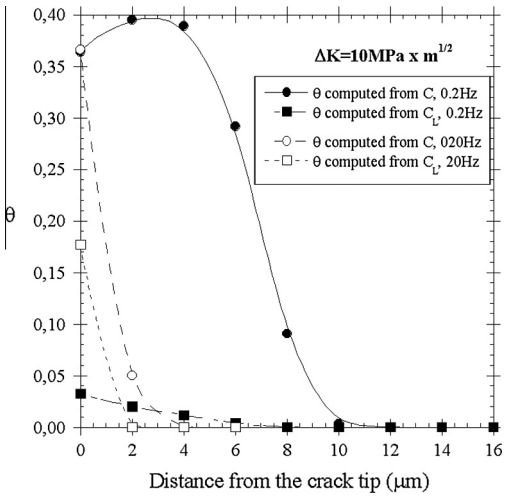

Fig. 13. Hydrogen coverage rate, determined for a similar crack advance (30 μm) from the total concentration $C(\theta)$ and the lattice concentration C_L (θ_L), at $\Delta K = 10\ \text{MPa} \times \text{m}^{1/2}$ for two loading frequencies, namely 0.2 and 20 Hz, a gaseous hydrogen pressure of 9 MPa, plotted as a function of the distance from the crack tip.

for the detrimental effect of dissolved hydrogen on the interface (reduction of the cohesion energy of the metallic lattice in presence of hydrogen). Only lattice diffusion as influenced by a stress field is considered. Hydrogen can furthermore be trapped on lattice defects assuming equilibrium between trapped and diffusible hydrogen. Finally the cyclic stress–strain behavior of the bulk material is described by an elasto-plastic constitutive law which is insensitive to the presence of hydrogen.

First, it has been shown that this model is able to predict at least qualitatively the deleterious effect generated by the penetration of hydrogen on the fatigue crack growth resistance for low gaseous hydrogen pressures and/or at $10\ \text{MPa}\sqrt{\text{m}} < \Delta K < 20\ \text{MPa}\sqrt{\text{m}}$. Additionally, it has been observed that at loading frequency 20 Hz and for different ΔK values and hydrogen pressures (from 0.09 MPa to 9 MPa), hydrogen lattice diffusion occurs over a distance limited to a few microns. When the loading frequency is significantly lowered (0.2 Hz), the distance affected by hydrogen diffusion along the crack path increases to 10 μm which allows suppose higher crack growth rates. However the model fails to accounting for the tremendous fatigue crack growth enhancement observed at high pressure for $\Delta K > 20\ \text{MPa}\sqrt{\text{m}}$. This suggests that the basic ingredients of the model are not sufficient and/or suited. This could be in particular the case of lattice diffusion. The role played in hydrogen transportation by mobile dislocations is also to be further investigated.

This finding can be related to the experimental results of Saintier et al. [45] based on SIMS measurements which indicate that the distance affected by hydrogen at the crack tip is of several orders larger than the distance estimated using lattice diffusion. These arguments emphasize the fact that lattice diffusion (controlled by the hydrostatic stress) cannot explain the hydrogen influence at high crack rate. It is necessary to enrich the model in order to capture the huge rate increase under high hydrogen pressure and high ΔK. It is also noteworthy that most of the relationships (Krom's equation, Kumnick and Johnson equation) used in the model have been established and/or validated for static and monotonic loading and should deserve a reassessment in the case of cyclic loading.

An additional effect of surface adsorption cannot be discarded either. Moro et al. [46] reached the conclusion that near-surface diffusible or adsorbed hydrogen atoms could be responsible for embrittlement observed under 30 MPa hydrogen pressure on a pipe steel. On-going work is precisely aiming in improving the predicting capacities of the model, especially in the high pressure domain. It is however noteworthy that Alvaro et al. [47,48] encountered a similar limitation when simulating the effect of gaseous hydrogen on the fracture toughness of a pipe steel. These authors particularly put in question the applicability of Sievert's law in these exposure conditions.

Acknowledgments

The funding from the "Région Poitou-Charentes" (Clara Moriconi PhD grant) is gratefully acknowledged. This work pertains to the French Government program "Investissements d'Avenir" (LABEX INTERACTIFS, reference ANR-11-LABX-0017-01).

References

[1] Petit J, Hénaff G, Sarrazin-Baudoux C. Environmentally-assisted fatigue in the gaseous atmosphere. In: Petit J, Scott P, editors. Comprehensive structural integrity. Elsevier; 2003. p. 211–80.
[2] San Marchi C, Somerday B. Technical reference on hydrogen compatibility of materials. In: Sandia National Laboratories, Albuquerque, New Mexico 87185 and Livermore, California 94550; 2008.
[3] Sun Z, Benoit G, Moriconi C, Hamon F, Halm D, Hamon F, Hénaff G. Fatigue crack propagation under gaseous hydrogen in a precipitation-hardened martensitic stainless steel. International Journal of Hydrogen Energy 4th Asian Bio-Hydrogen Symposium 2011; 36: p. 8641–4.
[4] Sun Z, Moriconi C, Benoit G, Halm D, Henaff G. Fatigue crack growth under high pressure of gaseous hydrogen in a 15-5ph martensitic stainless steel: influence of pressure and loading frequency. Metall Mater Trans Phys Metall Mater Sci 2013;44A:1320–30.
[5] Kirchheim R. Solid solution softening and hardening by mobile solute atoms with special focus on hydrogen. Scripta Mater 2012;67:767–70.
[6] Matsumoto R, Taketomi S, Matsumoto S, Miyazaki N. Atomistic simulations of hydrogen embrittlement. Int J Hydrogen Energy 2009;34:9576–84.
[7] Van der Ven A, Ceder G. The thermodynamics of decohesion. Acta Mater 2004;52:1223–35.
[8] Gurson AL. Continuum theory of ductile rupture by void nucleation and growth. 1. Yield criteria and flow rules for porous ductile media. J Eng Mater Technol Trans Asme 1977;99:2–15.
[9] Moes N, Dolbow J, Belytschko T. A finite element method for crack growth without remeshing. Int J Numer Methods Eng 1999;46:131–50.
[10] Sukumar N, Moes N, Moran B, Belytschko T. Extended finite element method for three-dimensional crack modelling. Int J Numer Methods Eng 2000;48:1549–70.
[11] Dugdale DS. Yielding of steel sheets containing slits. J Mech Phys Solids 1960;8:100–4.
[12] Barenblatt G.I. The mathematical theory of equilibrium cracks in brittle fracture. In: Advances in applied mechanics. Elsevier; 1962. p. 55–129.
[13] Camacho GT, Ortiz M. Computational modelling of impact damage in brittle materials. Int J Solids Struct 1996;33:2899–938.
[14] Scheider I, Brocks W. Cohesive elements for thin-walled structures. Comput Mater Sci 2006;37:101–9.
[15] Tvergaard V, Hutchinson JW. The relation between crack-growth resistance and fracture process parameters in elastic plastic solids. J Mech Phys Solids 1992;40:1377–97.
[16] Tvergaard V. Effect of fiber debonding in a whisker-reinforced metal. Mater Sci Eng Struct Mater Prop Microstruct Process 1990;125:203–13.
[17] Xu XP, Needleman A. Void nucleation by inclusion debonding in a crystal matrix. Model Simul Mater Sci Eng 1993;1:111–32.
[18] Olden V, Thaulow C, Johnsen R, Ostby E. A cohesive zone modeling approach to hydrogen induced stress cracking in 25%CR duplex stainless steel. In: Proceedings of the 26th international conference on offshore mechanics and arctic engineering, vol 4. AMER Soc Mechanical Engineers, New York; 2007. p. 57–65.
[19] Olden V, Thaulow C, Johnsen R, Ostby E. Cohesive zone modeling of hydrogen-induced stress cracking in 25% Cr duplex stainless steel. Scripta Mater 2007;57:615–8.
[20] Falkenberg R, Brocks W, Dietzel W, Scheider I. Simulation of stress-corrosion cracking by the cohesive model. In: Advances in fracture and damage mechanics Viii; 2010. p. 329–32.
[21] Charles Y, Gasperini M, Disashi J, Jouinot P. Numerical modeling of the disk pressure test up to failure under gaseous hydrogen. J Mater Process Technol 2012;212:1761–70.
[22] Ural A, Krishnan VR, Papoulia KD. A cohesive zone model for fatigue crack growth allowing for crack retardation. Int J Solids Struct 2009;46:2453–62.
[23] Bouvard JL, Chaboche JL, Feyel F, Gallerneau F. A cohesive zone model for fatigue and creep-fatigue crack growth in single crystal superalloys. Int J Fatigue 2009;31:868–79.

[24] Brinckmann S, Siegmund T. Computations of fatigue crack growth with strain gradient plasticity and an irreversible cohesive zone model. Eng Fract Mech 2008;75:2276–94.
[25] Needleman A. A continuum model for void nucleation by inclusion debonding. J Appl Mech Trans Asme 1987;54:525–31.
[26] Cornec A, Scheider I, Schwalbe KH. On the practical application of the cohesive model. Eng Fract Mech 2003;70:1963–87.
[27] Scheider I, Brocks W. The effect of the traction separation law on the results of cohesive zone crack propagation analyses. In: Advances in fracture and damage mechanics, Trans Tech Publications Ltd., Zurich-Uetikon; 2003. p. 313–18.
[28] Nguyen Q, Germain P, Suquet P. Continuum thermodynamics. J Appl Sci 1983;50:1010–20.
[29] Maugin G. The thermodynamics of nonlinear irreversible behaviors. An introduction. World Scientific; 1999.
[30] Olden V, Thaulow C, Johnsen R. Modelling of hydrogen diffusion and hydrogen induced cracking in supermartensitic and duplex stainless steels. Mater Des 2008;29:1934–48.
[31] Serebrinsky S, Carter EA, Ortiz M. A quantum-mechanically informed continuum model of hydrogen embrittlement. J Mech Phys Solids 2004;52:2403–30.
[32] Jiang DE, Carter EA. First principles assessment of ideal fracture energies of materials with mobile impurities: implications for hydrogen embrittlement of metals. Acta Mater 2004;52:4801–7.
[33] Sofronis P, McMeeking RM. Numerical-analysis of hydrogen transport near a blunting crack tip. J Mech Phys Solids 1989;37:317–50.
[34] Krom AHM, Koers RWJ, Bakker A. Hydrogen transport near a blunting crack tip. J Mech Phys Solids 1999;47:971–92.
[35] Oriani RA. The diffusion and trapping of hydrogen in steel. Acta Metall 1970;18:147–57.
[36] Johnson HH, Lin RW. Hydrogen deuterium trapping in iron. In: Hydrogen effects in metal, 1981. p. 3–23.
[37] Lin RW, Johnson HH. Plastic-deformation and hydrogen transport in metals. J Metals 1982;34:60.
[38] Kumnick AJ, Johnson HH. Deep trapping states for hydrogen in deformed iron. Acta Metall 1980;28:33–9.
[39] Hamon F. Modélisation du comportement mécanique enfissuration d'alliages aéronautiques. In: ENSMA, ENSMA, 2010. p. 180.
[40] Feih S. Development of a user element in ABAQUS for modelling of cohesive laws in composite structures. Roskilde: Riso National Laboratory; 2005.
[41] ASTM, E647-05 Standard Test Method for Measurement of Fatigue Crack Growth Rates. In: ASTM; 2008.
[42] Hirth J. Effects of hydrogen on the properties of iron and steel. Metall Mater Trans A 1980;11:861–90.
[43] Hénaff G, Petit J, Bouchet B. Environmental influence on the near-threshold fatigue crack propagation behaviour of a high-strength steel. Int J Fatigue 1992;14:211–8.
[44] Scheider I, Pfuff M, Dietzel W. Simulation of hydrogen assisted stress corrosion cracking using the cohesive model. Eng Fract Mech 2008;75:4283–91.
[45] Saintier N, Awane T, Olive JM, Matsuoka S, Murakami Y. Analyses of hydrogen distribution around fatigue crack on type 304 stainless steel using secondary ion mass spectrometry. Int J Hydrogen Energy 2011;36:8630–40.
[46] Moro I, Briottet L, Lemoine P, Andrieu E, Blanc C, Odemer G. Hydrogen embrittlement susceptibility of a high strength steel X80. Mater Sci Eng Struct Mater Prop Microstruct Process 2010;527:7252–60.
[47] Alvaro A, Olden V, Akselsen OM. 3D cohesive modelling of hydrogen embrittlement in the heat affected zone of an X70 pipeline steel – Part II. Int J Hydrogen Energy 2014;39:3528–41.
[48] Alvaro A, Olden V, Macadre A, Akselsen OM. Hydrogen embrittlement susceptibility of a weld simulated X70 heat affected zone under H2 pressure. Mater Sci Eng: A 2014;597:29–36.